RSC Advances

ROYAL SOCIETY OF CHEMISTRY

PAPER

View Article Online
View Journal | View Issue

Check for updates

Cite this: *RSC Adv.*, 2026, **16**, 3387

Silicon carbide/carbon nitride 1D/2D heterostructure towards superior visible-light-driven hydrogen generation from water splitting

Liting Wei,* Yinhu Yu, Jiao Jiao and Yangfang Wu

Received 20th October 2025
Accepted 6th January 2026

DOI: 10.1039/d5ra08027d

rsc.li/rsc-advances

Photocatalytic hydrogen evolution from water splitting is an attractive way to handle the energy crisis. Herein, a SiC/g-C_3N_4 1D/2D heterostructure photocatalyst was prepared *via* two-step polymerization of melamine on the surface of SiC nanowires. The incorporation of SiC nanowires induce the broadened light absorption, enlarged surface area and accelerated carrier separation and transfer across the SiC/g-C_3N_4 heterostructure. Consequently, the 1D/2D SiC/g-C_3N_4 exhibits higher H_2 generation rate (2250 μmol g^{-1} h^{-1}), which is 53 times higher than that of pristine g-C_3N_4 and superior to the already reported 0D/2D SiC/g-C_3N_4 photocatalysts. This work develops a novel 1D/2D heterojunction for the highly effective photocatalytic H_2 generation in the visible region.

1. Introduction

Hydrogen production *via* photocatalytic water splitting has been considered as a green, economical, and environmentally friendly way to achieve energy conversion.[1,2] At present, the energy conversion efficiency of solar-to-hydrogen (η_{STH}) is still below expectation, with the highest being ~1.16% under one-sun illumination.[3] The main obstacles are the lack of suitable photocatalysts which can simultaneously meet the following requirements:[4] (1) suitable band gap and band edge to absorb broadband light and meet the thermodynamic requirements of water splitting to produce hydrogen; (2) efficient separation and fast transfer of photo-generated electron–hole pairs. As a classic photocatalyst, g-C_3N_4 (CN) has received extensive attention due to low cost, nontoxicity, good chemical stability, and excellent electronic structure,[5–7] and shows potential applications in photocatalytic hydrogen production,[5,8] CO_2 reduction,[9,10] and pollutant degradation.[11–13]

However, the efficiency of pristine CN is still not satisfactory (0.5%)[14] due to the insufficient visible light absorption, the fast recombination of photogenerated electron–hole pairs and limited active sites.[15,16] It has been reported that coupling C_3N_4 with other semiconductors to construct the heterostructure should be a promising way to accelerate the charge transfer for enhanced photocatalytic activity.[17,18] One candidate of photocatalyst for hybridization of g-C_3N_4 is SiC, which has proper band edge and high carrier mobility.[19–22] To date, 0D SiC nanoparticles/2D CN nanosheets photocatalysts has been successfully prepared, which exhibit a lower photocatalytic hydrogen evolution rate under UV-vis light.[23–25] Compared with the point-to-face contact of 0D/2D interface, the line-to-face contact of 1D/2D interface is more beneficial to improve the catalytic performance, since its large interface contact area would provide sufficient charge transfer and trapping channels for the separation of photogenerated electron–hole pairs.[26] However, relatively scarce studies have been reported concerning construction of 1D/2D SiC/CN heterostructure. Moreover, the underlying structural factors responsible for the interfacial charge transfer have not been clearly identified.

In this work, we designed and synthesized CN nanosheets grown on SiC nanowires, which were self-assembled into a 1D/2D II-scheme heterostructure through the bridge of strong chemical bonds. The band-matched heterojunction not only improves the charge transfer at the interface, but also increases the light absorption and surface area. Thus, the SiC/CN demonstrates outstanding H_2 generation rate (2250 μmol g^{-1} h^{-1}) and apparent quantum yield (8.4% at 380 nm), which is 53 times higher than that of pristine CN. Accordingly, this type of heterostructure photocatalyst have a good potential in renewable clean energy conversion in terms of its superior photocatalytic activity, low cost as well as environmental friendliness.

2. Experimental

2.1 Preparation of 1D/2D SiC/CN composite photocatalyst

SiC nanowire was synthesized according to a previous report.[27] The SiC/CN composites were prepared by a two-step air etching method. In a typical synthesis procedure, 10.0 g of melamine and 5.0 mg of SiC were dispersed in 50 mL distilled water and sonicated for 1 h. Next, the mixture was transferred to a round flask to evaporate the excessive water at 100 °C under steady stirring, followed by annealing in air at 550 °C for 4 hours at a heating rate of 5 °C min^{-1}, and the obtained sample was

Department of Applied Chemistry, Yuncheng University, Yuncheng 044000, China. E-mail: weiliting_job@163.com

named as SiC/bulk CN. Subsequently, the obtained SiC/bulk CN was further annealed in an opened porcelain boat at 500 °C for 2 h at a ramping rate of 10 °C min^{-1}, and the derived sample was denoted as SiC/CN. SiC/CN composites with different mass ratios were synthesized by adding 1 mg, 5 mg, 10 mg SiC nanowire into 10.0 g of melamine, and were named as SiC/CN-01, SiC/CN-05, SiC/CN-10, respectively. As a reference sample, bare CN was prepared with the same condition as described above.

2.2 Characterization

The phase compositions of the samples were analyzed using a X-ray diffractometer (XRD) with Cu Kα radiation ($\lambda = 0.154$ nm) at 40 kV and 40 mA. The infrared absorption spectra were obtained using a Bruker Vertex 70 FTIR spectrophotometer with KBr as diluents. Scanning electron microscopy (SEM) images were acquired through a JSM-7800F instrument. The structural and morphological characterizations were examined with a transmission electron microscope (TEM, FEI Tecnai G^2 F30 S-Twin). X-ray photoelectron spectra (XPS) were acquired by a Kratos Axis Ultra X-ray spectrometer. Surface area and porosity measurement was carried out by N_2 adsorption on a Micromeritics ASAP 2020 plus instrument using the Brunauer–Emmett–Teller (BET) method. The UV-visible diffuse reflectance spectra (UV-vis) were obtained through a Hitachi U-4100 instrument equipped with a diffuse-reflectance accessory and with $BaSO_4$ as the reference. The photoluminescence (PL) images were acquired on a PTI QuantaMaster 40 steady-state fluorescence spectrophotometer at room temperature.

2.3 Photocatalytic H_2 production activity tests

Photocatalytic water splitting was carried out in a 110 mL Pyrex glass system equipped with a 300 W Xe lamp and a circulatory cooling water system to keep the reactor running near room temperature. Typically, 10 mg photocatalysts was dispersed in 80 mL ultrapure water containing 10 wt% triethanolamine (TEOA) as a sacrificial agent and 3 wt% Pt as a cocatalyst. Pt was *in situ* photodeposited on photocatalyst with $H_2PtCl_6 \cdot 6H_2O$ as a precursor. Before the light irradiation, the reaction cell was bubbled with Ar for 20 min to remove the dissolved air. The amount of H_2 was measured by a North Point NP-GC-901A gas chromatography (thermal conductivity detector, TDX-01 column, N_2 as the carrier gas). The apparent quantum yield (AQY) for hydrogen evolution was measured with band-pass filters (λ = 380, 420, 450, 500, 600 nm). The irradiation area was maintained at 10.17 cm^2, and AQY was calculated according to the given formula:

$$\begin{aligned}\text{AQY}\ (\%) &= \frac{N_{H_2}}{N_{p,\lambda}} \times 100 \\ &= \frac{2 \times \text{number of evolved } H_2 \text{ molecules}}{\text{number of incident photons}} \times 100\end{aligned}$$

3. Results and discussion

3.1 Structure, morphology and composition

The X-ray diffraction patterns reflect the phase structures of as-prepared photocatalysts. As shown in Fig. 1a, the peaks at 13.01° and 27.87° correspond to (100) and (002) diffraction planes of g-C_3N_4, respectively.[28] The (002) diffraction plane represents the graphite structure of typical peaks superimposed between aromatic groups, and (100) plane represents characteristic in-plane peak of the tri-*s*-triazine structure in CN. The (111), (220), (311) diffraction planes can be indexed to 3C-SiC (JCPDS No. 75-0254), and the small peak marked with SF is ascribed to the stacking faults.[29] After compositing, except for their regularly varying intensities due to different mass ratios, the diffraction peaks of individual CN and SiC remain unchanged, indicating that the hybrid process doesn't change the crystal structure of the two semiconductors. The signal of SiC for SiC/CN sample is very weak and only (220) diffraction peak is observed, mainly because of the low mass fraction of SiC.

The functional groups of the as-prepared photocatalysts can be analyzed from the FTIR spectra as shown in Fig. 1(b). The SiC nanowire exhibits a very strong absorption vibration peak at 796 cm^{-1}, which is the stretching vibration peak of Si–C bond. Theoretically, the stretching vibration peak of the Si–C bond is at 808 cm^{-1}. After the reaction at 550 °C for 4 h, the vibration peak of the sample shows a blue shift, which may be caused by the surface oxidation of SiC at high temperature. As a result, the electron cloud density of Si on Si–C bond shifts to O atom, making the electron cloud density of Si–C bond average, resulting in a decrease in the force constant of Si–C and a shift towards low wavenumber.[30,31] The sharp peaks at 474 cm^{-1}, 1051 cm^{-1} and 1089 cm^{-1} belong to the Si–O–Si asymmetric stretching vibration.[32] Besides, SiC/CN shows the similar FTIR spectra with CN, proving the undamaged molecular structure after compounding with SiC nanowires. For CN and SiC/CN, there are two distinct absorption peaks in the 810–890 cm^{-1} and 1195–1650 cm^{-1}, which correspond to the 1,3,5-substituted triazine cycle structure of CN and the typical stretching modes of C–N heterocycles, respectively.[33]

The morphology and microstructure of CN, SiC and SiC/CN-05 are shown in Fig. 2. CN and SiC exhibit a typical sheet-like structure and nanowire structure with the diameter about 30 nm (Fig. 2b), respectively. To clarify the morphology of SiC/CN and the interfacial interaction between SiC and CN in SiC/CN, TEM images and corresponding STEM elemental mapping of Si, C, N elements have been investigated (Fig. 2c–e). After the two-step polymerization of SiC and melamine, the SiC nanowires were anchored on the surface of CN nanosheets (shown in Fig. 2c). The interplanar distance of SiC nanowires is 0.25 nm (Fig. 2d), coinciding well with the (111) plane of SiC. The not clear lattice fringes in CN should result from the low crystallinity of CN. Furthermore, the HRTEM image displays that 2D CN nanosheets tightly combine with the surface of 1D SiC nanowires to form a heterojunction, which plays a significant role in the superior catalytic activity. The STEM image of

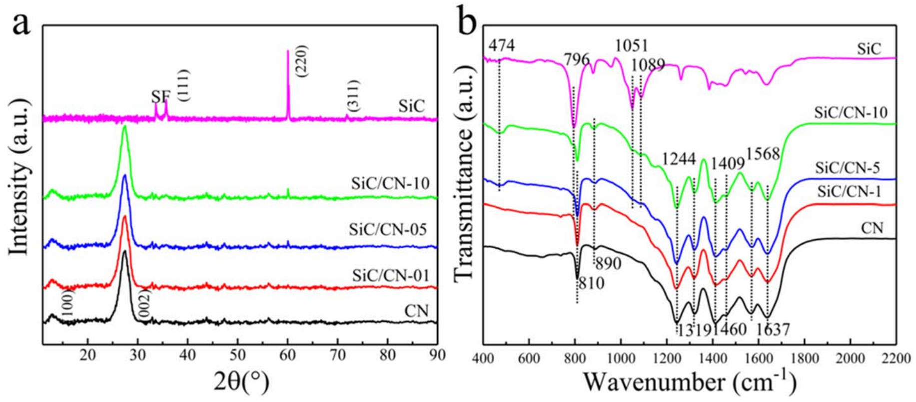

Fig. 1 (a) XRD patterns and (b) FTIR spectra of as-prepared photocatalysts.

the SiC/CN hybrids (Fig. S1) and corresponding elemental mapping of Si, C and N elements (Fig. 2e) evidently show that the nanowire contains Si and C elements, and nanosheets contains C and N elements, which further demonstrates the formation of 1D/2D SiC/CN heterojunction.

The XPS spectra in CN and SiC/CN composite are further investigated to analyze their surface chemical states and elemental composition. As shown in Fig. 3a, the SiC/CN sample displays the signals of C, N, O and Si. For the C 1s spectra of CN nanosheets and SiC/CN (Fig. 3b), the peaks at 286.2 and 288.3 eV could be indexed to C–NH$_2$ and N=C–N, respectively.[34] The binding energy of Si–C bond (283.8 eV) in SiC/CN is higher than that in SiC (283.2 eV),[35] suggesting the bridge of strong chemical bonds at the interface. N 1s spectrum of CN can be well fitted to four N species, *i.e.*, 398.4 eV for sp^2-hybridized nitrogen (C=N–C), 400.9 eV for amino functional groups possessing a hydrogen atom (C–N–H), 399.5 eV for N–(C)$_3$ and 404.0 eV for π excitation of the C=N conjugated structure.[36] The weak peaks at about 399.5 eV and 404.0 eV are assigned to the effects of sp^3-hybridized nitrogen including N–(C$_3$N$_3$)$_3$, HN–(C$_3$N$_3$)$_2$ and H$_2$N–C$_3$N$_3$ and π excitation, respectively.[37] When SiC is combined with CN, the binding energy of N is shifted towards the low binding energy due to the electron transfer from SiC to the N-containing group. This result provides a powerful evidence for the strong electron coupling at the 1D/2D interface. The Si 2p spectrum of SiC/CN-05 displays

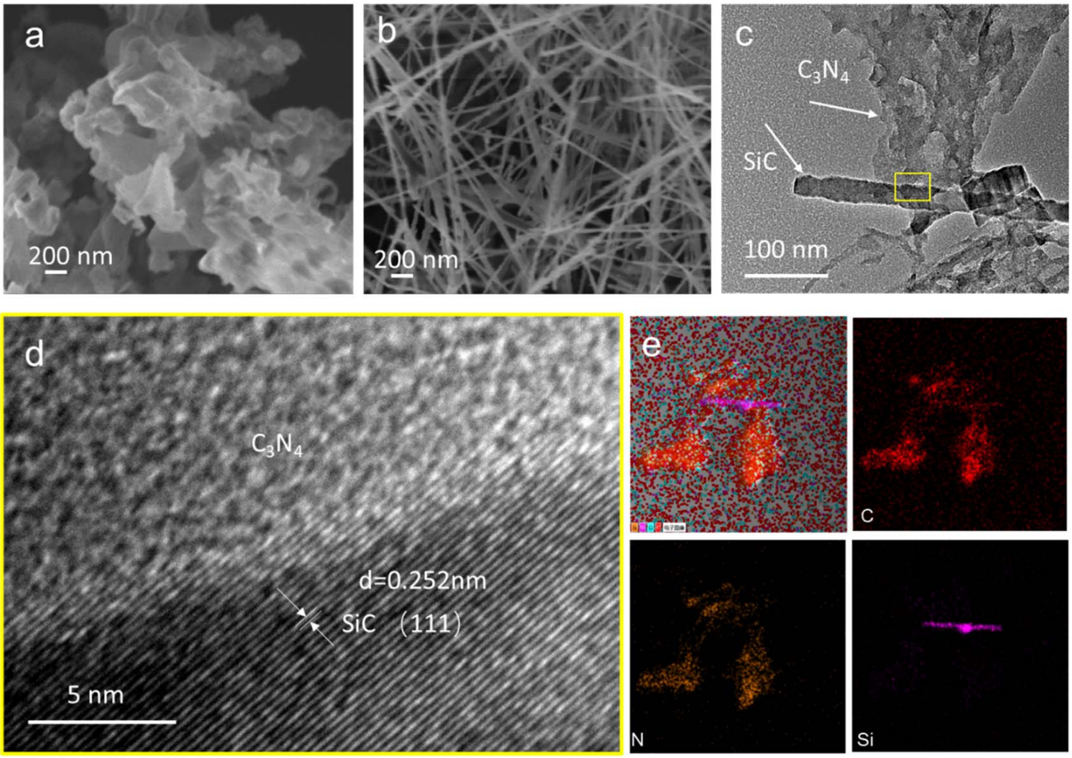

Fig. 2 SEM images of (a) CN and (b)SiC, (c) TEM (d) HRTEM and (e) EDX elemental mapping of SiC/CN-05 sample.

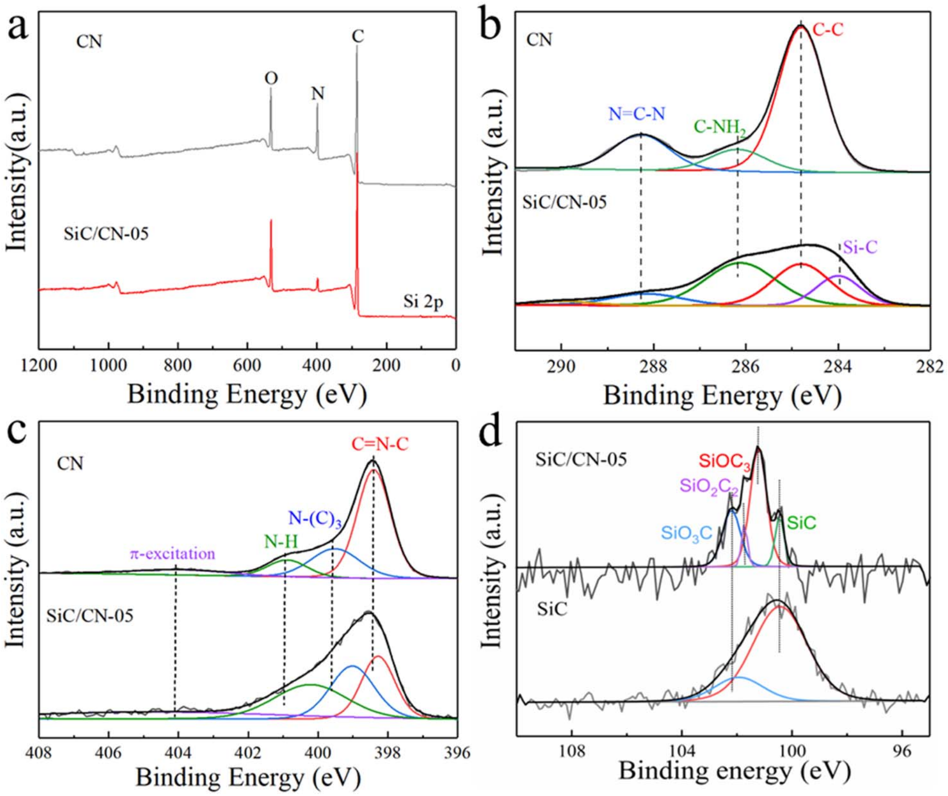

Fig. 3 (a) XPS survey spectra and high-resolution XPS spectra of (b) C 1s, (c) N 1s in CN and SiC/CN-05 and (d) Si 2p in SiC and SiC/CN-05.

the presence of Si–C bond and oxygen-contained groups including $SiOC_3$, SiO_2C_2 and SiO_3C. Compared with SiC, the peak area of Si–C bond decreases obviously, suggesting the surface oxidation of SiC during the synthesis of SiC/CN. Overall, the XPS characterization results further demonstrate that the intimate electronic coupling between 1D SiC and 2D CN can be formed, which could effectively strengthen the charge transfer.

Fig. 4 displays the nitrogen adsorption–desorption isotherms and corresponding pore size distribution curves of CN and SiC/CN-*x* samples. The N_2 adsorption–desorption isotherms of SiC and SiC/CN-*x* can be classified as type III isotherms and all has H3 hysteresis loops (Fig. 4a), implying the presence of mesopores, which is usually related to the slits originating from aggregates of plate-like CN.[38,39] With the addition of SiC nanowires, both the surface area and pore volume gradually increase, and reach the maximum when *x* is 5. When *x* continues to increase, the surface area and pore volume no longer change. Additionally, the sizes of the formed pores in CN and SiC/CN composite predominantly range from 1 to 50 nm, especially around 13 nm based on the BJH pore-size distribution as shown in Fig. 4b. Compared with CN, SiC/CN-05 shows obviously increased surface area (92.6 $m^2\ g^{-1}$) and

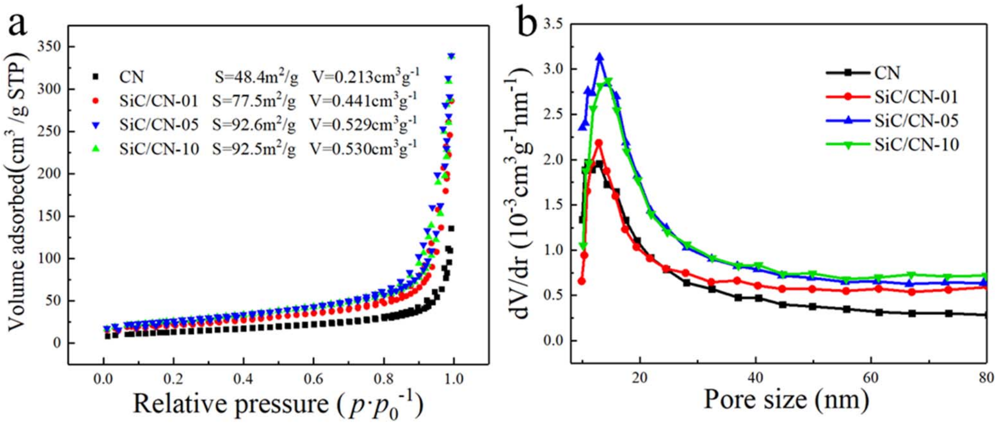

Fig. 4 (a) Nitrogen adsorption–desorption isotherms and (b) corresponding pore size distribution curves of CN and SiC/CN-*x*.

pore volume (0.529 cm^3 g^{-1}). This enhancement can be attributed to the effective prevention of CN agglomeration by SiC nanowires through extensive and intimate contact (Fig. 2). And it can provide more adsorption and reaction sites for the SiC/CN composites, which is conductive to their photocatalytic H_2 evolution.

3.2 Photocatalytic hydrogen evolution

The photocatalytic H_2-evolution activity of SiC, CN and SiC/CN composites were investigated in water with triethanolamine (TEOA) as a sacrificial reagent. As shown in Fig. 5a, the pristine CN shows a trace amount of H_2. Due to the poor conductivity, the excited electrons can't be effectively transferred to the active sites of the photocatalytic reaction, resulting in a high recombination rate of photo-excited carriers in pristine CN. Besides, SiC shows a negligible H_2-evolution activity. When heterojunction is formed between SiC and CN, the amount of H_2 significantly increases. The average H_2-evolution rate of SiC/CN-01, SiC/CN-05 and SiC/CN-10 can be calculated to be 362, 2250 and 885 μmol g^{-1} h^{-1}, which is 8, 53 and 21 times higher than pure CN (42 μmol g^{-1} h^{-1}), indicating the critical role of building efficient heterostructure. The photocatalytic activity is superior to the already reported 0D/2D SiC/g-C_3N_4 photocatalysts and within the middle range of previously reported g-C_3N_4-based photocatalysts, as shown in Table S1. The apparent quantum yield (AQY) of SiC/CN-05 reached 8.4% at $\lambda = 380$ nm (Fig. 5d and Table S2). Furthermore, the cyclic stability of photocatalysts is also crucial for the large-scale applications. Six-cycles hydrogen production experiment was conducted to investigate its stability. As shown in Fig. 5c, the H_2 production rate is kept for two cycles and exhibits a slight degradation (7.3%) after four cycles. In order to determine the cause of the decrease in catalytic activity, 2 mL of TEOA was added before the fifth cycle test began. It can be seen that the catalytic activity somewhat increases once the sacrificial agent is added. Therefore, the degradation in catalytic activity is potentially attributable to the overconsumption of the sacrificial reagent.

3.3 Photo physical and chemical properties

The optical properties of CN, SiC nanowires, and SiC/CN composites were investigated *via* UV-vis diffuse reflectance spectra (UV-vis DRS) (Fig. 6a). The SiC nanowires and CN show clear absorption edge around 544 nm and 440 nm, respectively. When CN was hybridized with the SiC, the extended light absorption can be observed. Table S3 summarizes the band gap energies and absorption edges of all synthesized samples. Among them, the absorption edge for SiC/CN-5 is 462 nm. The photoluminescence (PL) spectra of as-prepared catalysts in Fig. 6b are used to measure the recombination and transfer process of photo-generated carriers.[40] In general, the lower the intensity of PL emission peak, the lower the recombination of charge carriers. It can be seen that all samples exhibit a strong emission peak around 470 nm, which correspond to the band–band transition of the photo-induced carriers. Compared with

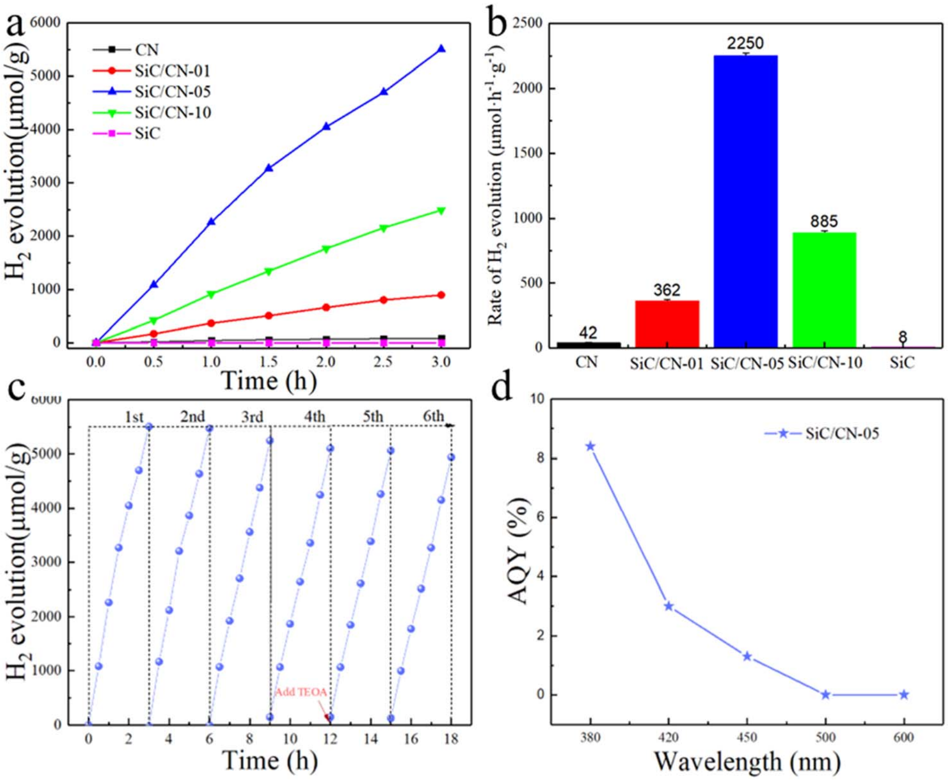

Fig. 5 (a) H_2 evolution and (b) average H_2 evolution rates of CN, SiC and SiC/CN-*x*. (c) Photocatalytic stability and (d) AQY of the SiC/CN-05 sample.

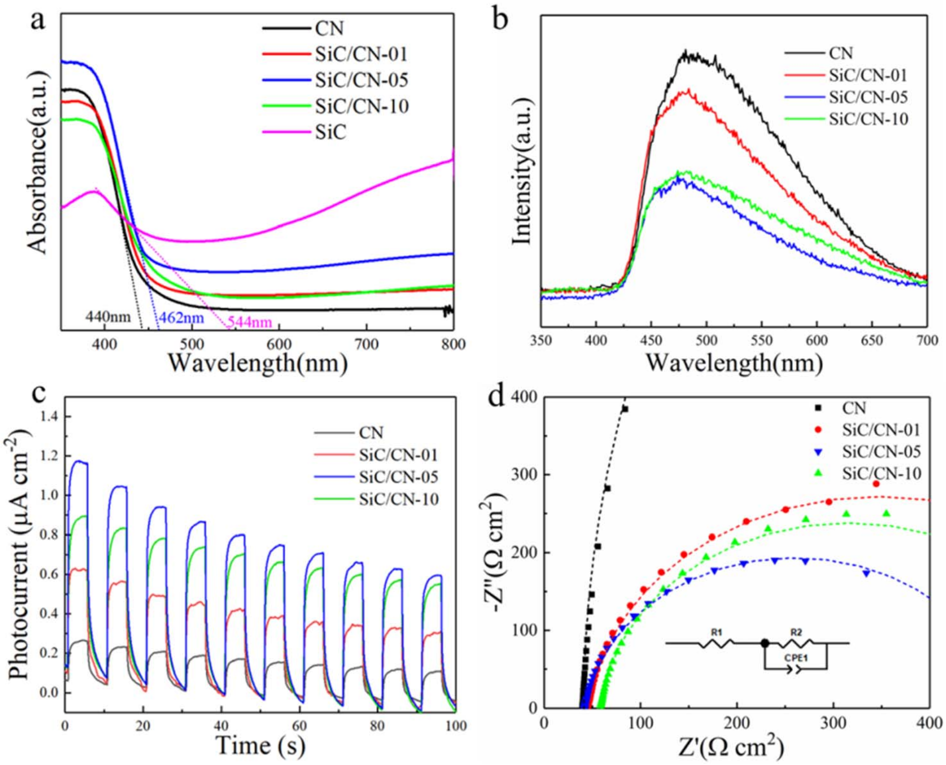

Fig. 6 (a) UV-vis diffuse reflectance, (b) PL spectra, (c) photocurrent response and (d) EIS of CN and SiC/CN-*x*.

pristine CN, SiC/CN heterostructure photocatalysts exhibit much weaker emission peak intensity, which indicated that the existence of SiC can effectively trap electrons and inhibit the geminate recombination of the carriers. Moreover, SiC/CN-05 sample with the weakest PL intensity proves the lowest recombination rate of photoinduced carriers, which is consistent with the H_2-evolution performance (Fig. 5).

Photoelectrochemical testing is an effective method to evaluate the separation and transfer efficiency of photogenerated electron–hole pairs. Fig. 7c indicates the transient photocurrent response of CN and series of SiC/CN-*x* samples. Compared with bare CN, SiC/CN-*x* displays much higher transient photocurrent, indicating that the SiC/CN heterostructure effectively enhances the separation of electron–hole pairs. Obviously, SiC/CN-05 sample exhibits the highest transient photocurrent. Besides, the electrochemical impedance spectroscopy (EIS) measurements were conducted to explore the charge transfer kinetics at the electrode/electrolyte interface. As shown in Fig. 7d, the EIS plots were fitted using an equivalent circuit including the series resistance (R_1) and charge transfer resistance at the interface between the electrode and the electrolyte (R_2). As displayed in Table S4, the values of R_2 for all SiC/CN-*x* samples are obviously lower than that of CN, suggesting that the introduction of SiC lowers the resistance of photogenerated charge transfer. The smallest R_2 can be found in the SiC/CN-05 sample; further increase of SiC mass ratio in the SiC/CN

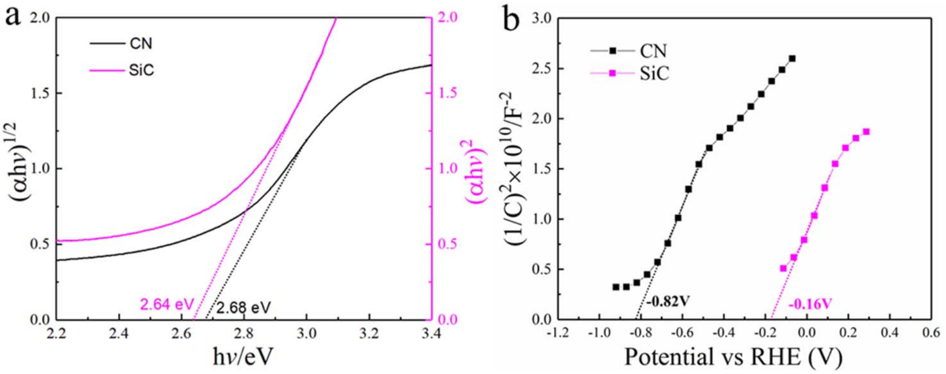

Fig. 7 (a) The band gap of CN and SiC, derived from the UV-vis spectra by Kubelka–Munk function. (b) Mott–Schottky (MS) plots of CN and SiC.

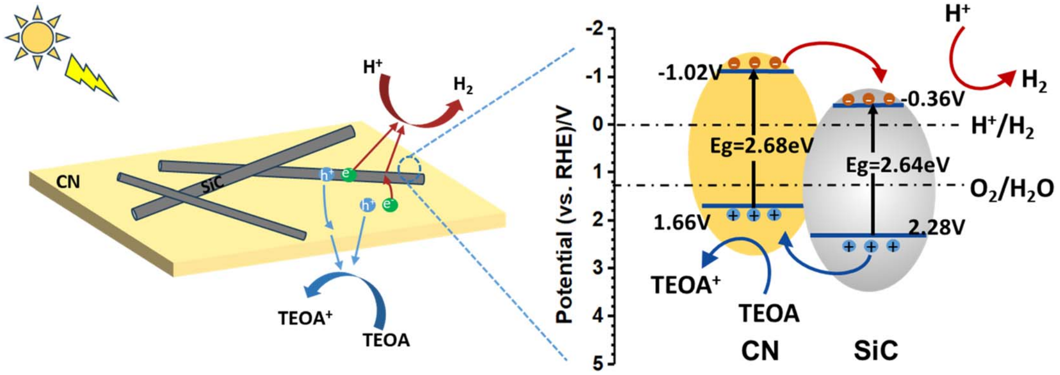

Fig. 8 The proposed mechanism of SiC/CN as a photocatalyst for water splitting.

composites leads to a larger charge transfer resistance. It is supposed that excessive addition of SiC could shield part of incident light, decreasing the light harvesting of CN to excite photogenerated carriers.[41]

To further understand the separation mechanism of photo-induced carriers, band gap energy and flat band potential were analyzed to construct the energy band structure. Calculated by the transformed Kubelka–Munk function (as shown in Fig. 6a), the band gap energies of CN and SiC are estimated to be 2.68 and 2.64 eV, respectively. The Mott–Schottky curves of CN and SiC have been obtained to analyze the flat band potential. As shown in Fig. 6b, both CN and SiC with the positive slopes represent n-type semiconductors endowed with the flat band potentials of −0.82 V and −0.16 V (*vs.* RHE), respectively. Semiconductor theory suggests that the flat band potential is equivalent to the Fermi level (E_f) and the conduction band (CB) potential of n-type semiconductor has difference of 0.2 V with their respective E_f.[42,43] Therefore, the CB of CN and SiC can be determined to be −1.02 and −0.36 V (*vs.* RHE), respectively. According to their band gap energies, their valence bands (VB) can be calculated to be 1.66 V and 2.28 V *vs.* RHE, respectively. Also, the MS plots of SiC/CN were measured (Fig. 6). From the above analysis, Fig. 8 proposes the energy-level diagrams of SiC and CN, and clearly illustrates the migration process of carriers. Upon light irradiation, the photo-excited electrons on the CB of CN will transfer to the CB of SiC. The recombination of photogenerated carriers is inhibited to a certain extent.

3.4 Photocatalytic mechanism

Based on the above discussion, we propose a potential mechanism to shed light on the photocatalytic process of 1D/2D SiC/CN composites (Fig. 8). After the *in situ* pyrolysis treatment, 1D/2D SiC/CN heterostructure had been successfully constructed. This unique heterostructure with intimate electronic coupling at the 1D/2D interface resulted in accelerated charge separation and transfer. Meanwhile, the existence of SiC broadened visible-light absorption and increase specific surface area. According to the previous UV-vis absorption spectrum and Mott Schottky results, the Fermi energy level, the conduction band (CB) as well as valence band (VB) can be determined. From the energy band structure of SiC and CN, when CN is attached to the SiC surface shown in Fig. 8, type II heterojunction is expected to appear at their interface. Under simulated visible light irradiation, photogenerated electrons stimulate from VB of CN and SiC to CB, leaving holes in the VB of both semiconductors. The photogenerated electrons in CN can rapidly transfer to the CB of SiC, together with the photogenerated electrons of SiC, participating in the generation of H_2. At the same time, the photoexcited holes would gather on the VBs of CN to oxidize the sacrificial reagent. With this specific 1D/2D heterostructure of the SiC/CN composite, photogenerated electron–hole pairs can be effectively separated and the photocatalytic hydrogen production activity can be greatly improved.

4. Conclusions

In summary, 1D SiC/2D g-C_3N_4 heterojunction photocatalysts have been successfully prepared by a simple two-step polymerization of melamine and SiC nanowires. *In situ* formation of type-II heterojunctions between SiC and g-C_3N_4 and their application in photocatalytic H_2 evolution was demonstrated. Under visible light irradiation, the H_2 evolution rate of the optimized catalysts SiC/CN-5 is as high as 2250 μmol g^{-1} h^{-1}, which is about 53 times higher than that of pristine g-C_3N_4. The reasons for the enhanced performance are as follows: (1) the incorporation of SiC nanowires broadens visible-light absorption and improves specific surface area; (2) the effective charge separation and transfer is enabled through the constructed type II heterojunction. This work develops a novel 1D/2D heterojunction photocatalyst and demonstrated its advantages for solar-driven water splitting.

Author contributions

Liting Wei: funding acquisition, data curation, formal analysis, investigation, writing – original draft, writing – review & editing. Yinhu Yu: formal analysis, investigation, writing – review & editing. Jiao Jiao: writing – review & editing. Yangfang Wu: writing – review & editing.

Conflicts of interest

The authors declare that they have no known competing financial interests or personal relationships that could have appeared to influence the work reported in this paper.

Data availability

Data supporting this article have been included as part of the supplementary information (SI). Supplementary information: STEM characterization of materials, M–S plot, fitting results of Nyquist plots, summary of photocatalytic activity; and apparent quantum yield calculations. See DOI: https://doi.org/10.1039/d5ra08027d.

Acknowledgements

This work is supported by the Doctoral Research Initiation Project of Yuncheng University, China (No. YXBQ-202516) and Basic Research Program of Yuncheng City, China (No. YCKJYD-202538).

References

1 A. Kudo and Y. Miseki, *Chem. Soc. Rev.*, 2009, **38**, 253–278.
2 X. Chen, S. Shen, L. Guo and S. S. Mao, *Chem. Rev.*, 2010, **110**, 6503–6570.
3 D. Zhao, Y. Wang, C.-L. Dong, Y.-C. Huang, J. Chen, F. Xue, S. Shen and L. Guo, *Nat. Energy*, 2021, **6**, 388–397.
4 M. G. Walter, E. L. Warren, J. R. McKone, S. W. Boettcher, Q. Mi, E. A. Santori and N. S. Lewis, *Chem. Rev.*, 2010, **110**, 6446–6473.
5 X. Wang, K. Maeda, A. Thomas, K. Takanabe, G. Xin, J. M. Carlsson, K. Domen and M. Antonietti, *Nat. Mater.*, 2009, **8**, 76–80.
6 S. Cao, J. Low, J. Yu and M. Jaroniec, *Adv. Mater.*, 2015, **27**, 2150–2176.
7 A. Kumar Singh, C. Das and A. Indra, *Coord. Chem. Rev.*, 2022, **465**, 214516.
8 L. Liu, Y. Qi, J. Hu, Y. Liang and W. Cui, *Appl. Surf. Sci.*, 2015, **351**, 1146–1154.
9 Z. Jiang, W. Wan, H. Li, S. Yuan, H. Zhao and P. K. Wong, *Adv. Mater.*, 2018, **30**, 1706108.
10 F. Raziq, L. Sun, Y. Wang, X. Zhang, M. Humayun, S. Ali, L. Bai, Y. Qu, H. Yu and L. Jing, *Adv. Energy Mater.*, 2018, **8**, 1701580.
11 L. Ji, L. Yan, M. Chao, M. Li, J. Gu, M. Lei, Y. Zhang, X. Wang, J. Xia, T. Chen, Y. Nie and T. Chen, *Small*, 2021, **17**, e2007122.
12 J. Cai, J. Huang, S. Wang, J. Iocozzia, Z. Sun, J. Sun, Y. Yang, Y. Lai and Z. Lin, *Adv. Mater.*, 2019, **31**, e1806314.
13 Q. Li, N. Zhang, Y. Yang, G. Wang and D. H. Ng, *Langmuir*, 2014, **30**, 8965–8972.
14 F. Raziq, Y. Qu, X. Zhang, M. Humayun, J. Wu, A. Zada, H. Yu, X. Sun and L. Jing, *J. Phys. Chem. C*, 2015, **120**, 98–107.
15 K. Li, Z. Zeng, L. Yan, M. Huo, Y. Guo, S. Luo and X. Luo, *Appl. Catal., B*, 2016, **187**, 269–280.
16 Q. Han, B. Wang, J. Gao, Z. Cheng, Y. Zhao, Z. Zhang and L. Qu, *ACS Nano*, 2016, **10**, 2745–2751.
17 S. Gong, Z. Jiang, P. Shi, J. Fan, Q. Xu and Y. Min, *Appl. Catal., B*, 2018, **238**, 318–327.
18 D. Kim and K. Yong, *Appl. Catal., B*, 2021, **282**, 119538.
19 G. Tuci, Y. Liu, A. Rossin, X. Guo, C. Pham, G. Giambastiani and C. Pham-Huu, *Chem. Rev.*, 2021, **121**, 10559–10665.
20 J. Chen, H. Pan, H. Hou, H. Li, J. Yang and L. Wang, *Chem. Eng. J.*, 2017, **323**, 444–454.
21 H. Li, J. Chen, H. Hou, H. Pan, X. Ma, J. Yang, L. Wang and J. C. Crittenden, *Water Res.*, 2017, **126**, 274–284.
22 Y. Peng, L. Wang, Q. Luo, Y. Cao, Y. Dai, Z. Li, H. Li, X. Zheng, W. Yan, J. Yang and J. Zeng, *Chem*, 2018, **4**, 613–625.
23 Z. Du, P. Sun, K. Wu, X. Zheng, X. Zhang, J. Huang, D. Sun, Y. Zheng and Q. Li, *Energy Technol.*, 2019, **7**, 1900017.
24 H. Xu, Z. Gan, W. Zhou, Z. Ding and X. Zhang, *RSC Adv.*, 2017, **7**, 40028–40033.
25 B. Wang, J. Zhang and F. Huang, *Appl. Surf. Sci.*, 2017, **391**, 449–456.
26 B. X. Zhou, S. S. Ding, K. X. Yang, J. Zhang, G. F. Huang, A. Pan, W. Hu, K. Li and W. Q. Huang, *Adv. Funct. Mater.*, 2020, **31**, 2009230.
27 L. Su, H. Wang, M. Niu, X. Fan, M. Ma, Z. Shi and S. W. Guo, *ACS Nano*, 2018, **12**, 3103–3111.
28 Y. Zhu, T. Ren and Z. Yuan, *ACS Appl. Mater. Interfaces*, 2015, **7**, 16850–16856.
29 Y. Zhang, M. Ishimaru, T. Varga, T. Oda, C. Hardiman, H. Xue, Y. Katoh, S. Shannon and W. J. Weber, *Phys. Chem. Chem. Phys.*, 2012, **14**, 13429–13436.
30 J. Sun, J. Li, G. Sun, B. Zhang, S. Zhang and H. Zhai, *Ceram. Int.*, 2002, **28**, 741–745.
31 Y. Li, X. Lv, J. Lu and J. Li, *J. Phys. Chem. C*, 2010, **114**, 21770–21774.
32 Q. Hu, H. Suzuki, H. Gao, H. Araki, W. Yang and T. Noda, *Chem. Phys. Lett.*, 2003, **378**, 299–304.
33 G. Zhang, J. Zhang, M. Zhang and X. Wang, *J. Mater. Chem.*, 2012, **22**, 8083–8091.
34 F. Xue, Y. Si, M. Wang, M. Liu and L. Guo, *Nano Energy*, 2019, **62**, 823–831.
35 J. Pan, Y. Zhang, Y. Guan, Y. Yan, H. Tang, X. Liu, M. Wang and X. Wei, *Appl. Surf. Sci.*, 2022, **579**, 152171.
36 M. Wang, Z. Wu and L. Dai, *J. Electroanal. Chem.*, 2015, **753**, 16–20.
37 Y. Zang, L. Li, Y. Xu, Y. Zuo and G. Li, *J. Mater. Chem. A*, 2014, **2**, 15774–15780.
38 J. Shi, J. Ye, Q. Li, Z. Zhou, H. Tong, G. Xi and L. Guo, *Chemistry*, 2012, **18**, 3157–3162.
39 Z. Zou, J. Ye, K. Sayama and H. Arakawa, *Nature*, 2001, **414**, 625–627.
40 J. Zhang, L. Qi, J. Ran, J. Yu and S. Z. Qiao, *Adv. Energy Mater.*, 2014, **4**, 1301925.
41 J. Zhang and F. Huang, *Appl. Surf. Sci.*, 2015, **358**, 287–295.
42 X. Li, J. Yu, J. Low, Y. Fang, J. Xiao and X. Chen, *J. Mater. Chem. A*, 2015, **3**, 2485–2534.
43 L. Wei, L. Zhang, L. Li and J. Su, *Int. J. Hydrogen Energy*, 2024, **82**, 64–72.